V International Conference on Computational Methods for Coupled Problems in Science and Engineering
COUPLED PROBLEMS 2013
S. Idelsohn, M. Papadrakakis and B. Schrefler (Eds)

FAST SOLVERS AND EFFICIENT NUMERICAL CFD TECHNIQUES FOR DYNAMIC POROUS MEDIA PROBLEMS

S. TUREK*, A. OBAID* AND B. MARKERT†

*Institute of Applied Mathematics (LS3)
Dortmund University of Technology
Vogelpothsweg 87, 44227 Dortmund, Germany
e-mail: {stefan.turek,aobaid}@math.tu-dortmund.de, web page:
http://www.mathematik.tu-dortmund.de/lsiii/cms/de/lehrstuhl3.html

†Institute of Applied Mechanics (CE)
University of Stuttgart
Pfaffenwaldring 7, 70569 Stuttgart, Germany
e-mail: bernd.markert@mechbau.uni-stuttgart.de - Web page:
http://www.mechbau.uni-stuttgart.de/ls2/index.en.html

Key words: Multigrid solver , Porous media dynamics , Coupled problem , Monolithic solution , Fully implicit , Finite element method , CFD

Abstract. We present a fully implicit, monolithic finite element solution scheme to efficiently solve the governing set of differential algebraic equations of incompressible poro-elastodynamics. Thereby, we proceed from a two-dimensional, biphasic, saturated porous medium model with intrinsically coupled and incompressible solid and fluid constituents. Our approach, motivated by well-accepted CFD techniques and originally developed for the efficient simulation of incompressible flow problems, is characterized by the following aspects: (1) a special treatment of the algebraically coupled volume balance equation leading to a reduced form of the boundary conditions; (2) usage of a higher-order accurate mixed LBB-stable finite element pair with piecewise discontinuous pressure for the spatial discretization; (3) application of the fully implicit 2nd-order Crank-Nicolson scheme for the time discretization; (4) use of a special fast multigrid solver for the resulting discrete linear equation system. For the purpose of validation and to expose the merits and benefits of our new solution strategy in comparison to other established approaches, canonical one- and two-dimensional wave propagation problems are solved. Finally, a large-scale, dynamic soil-structure interaction problem serves to reveal the efficiency of the special multigrid solver in combination with the chosen finite element discretization.

1 Governing Equations

In the framework of the Theory of Porous Media (TPM) [4], we proceed from a continuum-mechanical description of a fluid-filled porous body consisting of a solid matrix saturated by a single pore fluid. Thereby, the binary aggregate is treated as a macroscopic mixture φ with overlaid and interacting but de facto immiscible solid and fluid constituents φ^α ($\alpha = S$: solid; $\alpha = F$: fluid), so that $\varphi = \varphi^S \cup \varphi^F$ at any macroscopic spatial point $\mathbf{x}(t)$ at any time $t \in [t_0, T]$. The local composition of the biphasic continuum is described by volume fractions $n^\alpha(\mathbf{x}, t) := \mathrm{d}v^\alpha / \mathrm{d}v \in (0, 1)$ of φ^α (n^S : solidity; n^F : porosity) defined as the ratios of the partial to the total volume elements of φ. Assuming fully saturated conditions, the saturation constraint obviously yields $\sum_\alpha n^\alpha = n^S + n^F = 1$. Closely related is the introduction of two density functions, namely an effective density $\rho^{\alpha R}(\mathbf{x}, t)$ and a partial density $\rho^\alpha(\mathbf{x}, t)$ relating the local mass of φ^α to the partial or the bulk volume element. The considered biphasic model excludes thermal effects as well as mass exchanges (inert φ^α) and proceeds from intrinsically incompressible constituents ($\rho^{\alpha R} = \text{const.}$). In particular, the arising purely mechanical, binary model with $\alpha = \{S, F\}$ is governed by the following constituent balance equations:

$$\rho^S (\mathbf{v}_S)'_S = \operatorname{div} \mathbf{T}^S_E - n^S \operatorname{grad} p + \rho^S \mathbf{b} + \frac{(n^F)^2 \, \gamma^{FR}}{k^F} (\mathbf{v}_F - \mathbf{v}_S) \tag{1}$$

$$\rho^F (\mathbf{v}_F)'_S + \rho^F (\operatorname{grad} \mathbf{v}_F)(\mathbf{v}_F - \mathbf{v}_S) = \operatorname{div} \mathbf{T}^F_E - n^F \operatorname{grad} p + \rho^F \, \mathbf{b} - \frac{(n^F)^2 \, \gamma^{FR}}{k^F} (\mathbf{v}_F - \mathbf{v}_S) \tag{2}$$

$$\operatorname{grad} n^F \cdot \mathbf{v}_F + \operatorname{grad} n^S \cdot \mathbf{v}_S + n^F \operatorname{div} \mathbf{v}_F + n^S \operatorname{div} \mathbf{v}_S = 0 \tag{3}$$

Here, $\operatorname{div}(\bullet)$ is the divergence operator related to $\operatorname{grad}(\bullet)$, $\mathbf{T}^\alpha_E = (\mathbf{T}^\alpha_E)^T$ is the symmetric extra stress assuming non-polar constituents, $\mathbf{b}$ is the mass-specific body force acting on the overall aggregate. n^S and n^F are assumed to be constant, which is acceptable for the small deformation case, such that the blue terms are dropped out. Furthermore, proceeding from a geometrically linear description, the (red) nonlinear convective term becomes negligible. To continue with linear PDEs, the pore fluid is assumed to be Newtonian and incompressible leading to the following relation:

$$\operatorname{div} \mathbf{T}^F_E = \nu \Delta \mathbf{v}_F \tag{4}$$

In spite of its negligible influence (cf. [6]) in all our performed numerical tests so far, this term containing the (small) fluid viscosity is nevertheless considered in our subsequent discretization and solution approaches, particularly in view of future large scale simulations which shall be able to involve all physically relevant effects. Restricting the presentation

to the small strain regime, the solid extra stress is determined by the Hookean elasticity law

$$\mathbf{T}_E^S = 2\mu^S\,\boldsymbol{\varepsilon}_S + \lambda^S\,(\boldsymbol{\varepsilon}_S \cdot \mathbf{I})\,\mathbf{I} \qquad \text{with} \qquad \boldsymbol{\varepsilon}_S = \tfrac{1}{2}\,(\operatorname{grad}\mathbf{u}_S + \operatorname{grad}^T\mathbf{u}_S) \tag{5}$$

as the geometrically linear solid strain tensor and μ^S, λ^S being the macroscopic Lamé constants of the porous solid matrix. Note that the chosen primary unknowns for this set of PDE are $\mathbf{u}_S$, $\mathbf{v}_F$ and p. Hence, $\mathbf{v}_S(\mathbf{u}_S)$ as well as $\mathbf{T}_E^S(\mathbf{u}_S)$, $\mathbf{T}_E^F(\mathbf{v}_F)$, $n^S(\mathbf{u}_S)$ and $n^F(\mathbf{u}_S)$ represent the secondary variables of the problem. Additionally, a reduction in the order of the PDE to order-one in time is achieved using

$$(\mathbf{u}_S)'_S = \mathbf{v}_S \tag{6}$$

which eliminates the second time derivative of the solid displacement from (1), and allows the applicability of a wide range of fundamental time-stepping algorithms. This is a short presentation and for a more detailed discussion, the interested reader is referred to [2, 3, 7] and the citations therein.

2 Weak formulation and discretization in space and time

Our subsequent variational form of the **uv**p approach, inspired by weak formulations that are typical in the CFD community for treating the incompressible Navier-Stokes equations, is created by multiplying (1)-(3) with the displacement test function $\delta\mathbf{u}_S$, the velocity test function $\delta\mathbf{v}_F$, the pressure test function δp, integrating over the whole domain Ω and performing partial integrations. Finally, we obtain the following weak form, which is similar to the standard one for porous media (see, for instance, page 1349 of [7]):

$$\begin{aligned}&\int_\Omega \operatorname{grad}\delta\mathbf{u}_S \colon \mathbf{T}_E^S\,\mathrm{d}v - \int_\Omega \frac{(n^F)^2\,\gamma^{FR}}{k^F}\,\delta\mathbf{u}_S\cdot\mathbf{v}_F\,\mathrm{d}v - \int_\Omega n^S \operatorname{div}\delta\mathbf{u}_S\; p\,\mathrm{d}v + \\ &\int_\Omega \frac{(n^F)^2\,\gamma^{FR}}{k^F}\,\delta\mathbf{u}_S\cdot\mathbf{v}_S\,\mathrm{d}v + \int_\Omega \rho^S\delta\mathbf{u}_S\cdot\left\{(\mathbf{v}_S)'_S - \mathbf{b}\right\}\mathrm{d}v = \int_{\Gamma_{\mathbf{t}^S}} \delta\mathbf{u}_S\cdot\bar{\mathbf{t}}^S\,\mathrm{d}a\end{aligned} \tag{7}$$

$$\begin{aligned}&\int_\Omega \nu\operatorname{grad}\delta\mathbf{v}_F \colon \operatorname{grad}\mathbf{v}_F\,\mathrm{d}v + \int_\Omega \frac{(n^F)^2\,\gamma^{FR}}{k^F}\,\delta\mathbf{v}_F\cdot\mathbf{v}_F\,\mathrm{d}v - \int_\Omega n^F \operatorname{div}\delta\mathbf{v}_F\; p\,\mathrm{d}v - \\ &\int_\Omega \frac{(n^F)^2\,\gamma^{FR}}{k^F}\,\delta\mathbf{v}_F\cdot\mathbf{v}_S\,\mathrm{d}v + \int_\Omega \rho^F\delta\mathbf{v}_F\cdot\left\{(\mathbf{v}_F)'_S - \mathbf{b}\right\}\mathrm{d}v = \int_{\Gamma_{\mathbf{t}^F}} \delta\mathbf{v}_F\cdot\bar{\mathbf{t}}^F\,\mathrm{d}a\end{aligned} \tag{8}$$

$$\int_\Omega n^S\delta p\,\operatorname{div}\mathbf{v}_S\,\mathrm{d}v + \int_\Omega n^F\delta p\,\operatorname{div}\mathbf{v}_F\,\mathrm{d}v = 0 \tag{9}$$

Here, the red-colored terms represent slight differences to [7], namely the additional fluid viscosity term and the natural shape of the weak form of the volume balance. Finally, we multiply (6) with $\delta\mathbf{u}_S$ and integrate over Ω:

$$\int_\Omega \delta\mathbf{u}_S\cdot\left\{(\mathbf{u}_S)'_S - \mathbf{v}_S\right\}\mathrm{d}v = 0 \tag{10}$$

The boundary $\Gamma = \partial\Omega$ is divided into Dirichlet (essential) and Neumann (natural) boundaries, respectively, resulting in $\Gamma = \Gamma_{\mathbf{u}_S} \cup \Gamma_{\mathbf{t}^S}$ for the solid momentum balance and in $\Gamma = \Gamma_{\mathbf{v}_F} \cup \Gamma_{\mathbf{t}^F}$ for the fluid momentum balance, wherein the tractions are defined as:

$$\mathbf{t}^S = \left(\mathbf{T}_E^S - n^S p \mathbf{I}\right) \cdot \mathbf{n}\,, \qquad \mathbf{t}^F = \nu \frac{\partial \mathbf{v}_F}{\partial \mathbf{n}} - n^F p \mathbf{n} \tag{11}$$

Keep in mind that due to the fact that the pressure (as Lagrange multiplier regarding the incompressibility constraint) provides typically less regularity than displacement and velocity, the pressure derivatives in the weak formulation have been eliminated by partial integration. For the same reason and as usual for the treatment of the incompressible Navier-Stokes equations, no integration by parts has been carried out in (9).

Using such a weak form, which avoids derivatives acting on the pressure functions, one can use standard FEM pairs for velocity/displacement and pressure as typical for incompressible flow problems, which are based on piecewise discontinuous pressure approximations (as shown in Figure 1), and the boundary conditions are imposed in a slightly modified way in which the fully drained boundaries are represented by the typical CFD 'Do-nothing' (see [5]) boundary condition ($\mathbf{t}^{\mathrm{F}} = 0$) while the volume effluxes and values for the pressure as boundary conditions are not needed anymore. Therefore, we can choose the boundary conditions independently. As a candidate for LBB-stable Stokes elements, we apply in the following (2D) simulations the well-known (non-parametric) Q2/P1 element, that means biquadratic velocities and displacements and piecewise linear (discontinuous) pressure approximations (cf. [11]), which belongs currently to the 'best' FEM choices for incompressible flow problems with respect to efficiency, accuracy and robustness.

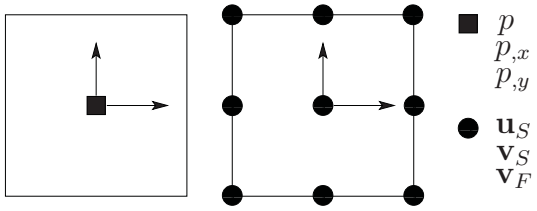

Figure 1: The discontinuous linear pressure element P1 (left) and the 9-node Lagrange biquadratic element Q2 (right) that we use for our $\mathbf{uv}p(3)$-TR method.

Next, based on the discretization with the introduced FEM spaces, equations (7)-(10) can be written in the following matrix-vector notation:

$$\mathbf{M}\dot{\mathbf{y}} + \mathbf{K}\mathbf{y} = \mathbf{f} \tag{12}$$

In more detail with mass and stiffness matrices and right hand side vectors, one obtains

$$\underbrace{\begin{pmatrix} \mathbf{M}_{\mathbf{v}_S\mathbf{u}_S} & \mathbf{0} & \mathbf{0} & \mathbf{0} \\ \mathbf{0} & \mathbf{M}_{\mathbf{u}_S\mathbf{v}_S} & \mathbf{0} & \mathbf{0} \\ \mathbf{0} & \mathbf{0} & \mathbf{M}_{\mathbf{v}_F\mathbf{v}_F} & \mathbf{0} \\ \mathbf{0} & \mathbf{0} & \mathbf{0} & 0 \end{pmatrix}}_{\mathbf{M}} \underbrace{\begin{pmatrix} \dot{\mathbf{u}}_S \\ \dot{\mathbf{v}}_S \\ \dot{\mathbf{v}}_F \\ \dot{p} \end{pmatrix}}_{\dot{\mathbf{y}}} + \underbrace{\begin{pmatrix} \mathbf{0} & \mathbf{K}_{\mathbf{v}_S\mathbf{v}_S} & \mathbf{0} & \mathbf{0} \\ \mathbf{K}_{\mathbf{u}_S\mathbf{u}_S} & \mathbf{K}_{\mathbf{u}_S\mathbf{v}_S} & \mathbf{K}_{\mathbf{u}_S\mathbf{v}_F} & \mathbf{K}_{\mathbf{u}_Sp} \\ \mathbf{0} & \mathbf{K}_{\mathbf{v}_F\mathbf{v}_S} & \mathbf{K}_{\mathbf{v}_F\mathbf{v}_F} & \mathbf{K}_{\mathbf{v}_Fp} \\ \mathbf{0} & \mathbf{K}_{p\mathbf{v}_S} & \mathbf{K}_{p\mathbf{v}_F} & 0 \end{pmatrix}}_{\mathbf{K}} \underbrace{\begin{pmatrix} \mathbf{u}_S \\ \mathbf{v}_S \\ \mathbf{v}_F \\ p \end{pmatrix}}_{\mathbf{y}} = \underbrace{\begin{pmatrix} \mathbf{0} \\ \mathbf{f}_{\mathbf{u}_S} + \mathbf{b}_S \\ \mathbf{f}_{\mathbf{v}_F} + \mathbf{b}_F \\ \mathbf{0} \end{pmatrix}}_{\mathbf{f}} \tag{13}$$

with the following matrices and right hand side vectors:

$$\begin{aligned}
\mathbf{K}_{\mathbf{u}_S\mathbf{u}_S} &= \int_\Omega \operatorname{grad}\delta\mathbf{u}_S \colon \mathbf{T}_E^S \,\mathrm{d}v\,, \quad \mathbf{K}_{\mathbf{u}_S\mathbf{v}_S} = \int_\Omega \frac{(n^F)^2\,\gamma^{FR}}{k^F}\,\delta\mathbf{u}_S\cdot\mathbf{v}_S\,\mathrm{d}v \\
\mathbf{K}_{\mathbf{u}_S\mathbf{v}_F} &= -\int_\Omega \frac{(n^F)^2\,\gamma^{FR}}{k^F}\,\delta\mathbf{u}_S\cdot\mathbf{v}_F\,\mathrm{d}v\,, \quad \mathbf{K}_{\mathbf{u}_Sp} = -\int_\Omega n^S \operatorname{div}\delta\mathbf{u}_S\; p\,\mathrm{d}v \\
\mathbf{K}_{\mathbf{v}_S\mathbf{v}_S} &= -\int_\Omega \delta\mathbf{u}_S\cdot\mathbf{v}_S\,\mathrm{d}v\,, \quad \mathbf{K}_{\mathbf{v}_F\mathbf{v}_S} = -\int_\Omega \frac{(n^F)^2\,\gamma^{FR}}{k^F}\,\delta\mathbf{v}_F\cdot\mathbf{v}_S\,\mathrm{d}v \\
\mathbf{K}_{\mathbf{v}_F\mathbf{v}_F} &= \int_\Omega \nu\operatorname{grad}\delta\mathbf{v}_F \colon \operatorname{grad}\mathbf{v}_F\,\mathrm{d}v + \int_\Omega \frac{(n^F)^2\,\gamma^{FR}}{k^F}\,\delta\mathbf{v}_F\cdot\mathbf{v}_F\,\mathrm{d}v \\
\mathbf{K}_{\mathbf{v}_Fp} &= -\int_\Omega n^F \operatorname{div}\delta\mathbf{v}_F\; p\,\mathrm{d}v\,, \quad \mathbf{K}_{p\mathbf{v}_S} = \int_\Omega n^S\delta p\;\operatorname{div}\mathbf{v}_S\,\mathrm{d}v \\
\mathbf{K}_{p\mathbf{v}_F} &= \int_\Omega n^F\delta p\;\operatorname{div}\mathbf{v}_F\,\mathrm{d}v\,, \quad \mathbf{M}_{\mathbf{u}_S\mathbf{v}_S} = \int_\Omega \left\{n^S\rho^{SR}\right\}\delta\mathbf{u}_S\cdot(\mathbf{v}_S)'_S\,\mathrm{d}v \\
\mathbf{M}_{\mathbf{v}_S\mathbf{u}_S} &= \int_\Omega \delta\mathbf{u}_S\cdot(\mathbf{u}_S)'_S\,\mathrm{d}v\,, \quad \mathbf{M}_{\mathbf{v}_F\mathbf{v}_F} = \int_\Omega \left\{n^F\rho^{FR}\right\}\delta\mathbf{v}_F\cdot(\mathbf{v}_F)'_S\,\mathrm{d}v \\
\mathbf{f}_{\mathbf{u}_S} &= \int_{\Gamma_{\mathbf{t}^S}} \delta\mathbf{u}_S\cdot\bar{\mathbf{t}}^S\,\mathrm{d}a\,, \quad \mathbf{f}_{\mathbf{v}_F} = \int_{\Gamma_{\mathbf{t}^F}} \delta\mathbf{v}_F\cdot\bar{\mathbf{t}}^F\,\mathrm{d}a \\
\mathbf{b}_S &= \int_\Omega \left\{n^S\rho^{SR}\right\}\delta\mathbf{u}_S\cdot\mathbf{b}\,\mathrm{d}v\,, \quad \mathbf{b}_F = \int_\Omega \left\{n^F\rho^{FR}\right\}\delta\mathbf{v}_F\cdot\mathbf{b}\,\mathrm{d}v
\end{aligned} \tag{14}$$

In the next step, regarding the time integration, equations (12) or (13) are treated in a monolithic implicit way leading to a fully coupled system. In our approach, we apply the standard one-step θ-scheme to these systems, which leads to

$$\mathbf{M}\frac{\mathbf{y}_{n+1}-\mathbf{y}_n}{\Delta t} + \theta\mathbf{K}\mathbf{y}_{n+1} = -(1-\theta)\,\mathbf{K}\mathbf{y}_n + \theta\mathbf{f}_{n+1} + (1-\theta)\mathbf{f}_n\,. \tag{15}$$

In the subsequent more detailed description, the red-colored continuity equation and the blue-colored pressure p as corresponding Lagrange multiplier are treated fully implicitly

($\theta = 1$) (cf. [11]).

$$\begin{pmatrix} \mathbf{M}_{\mathbf{v}_S\mathbf{u}_S} & \theta\Delta t\mathbf{K}_{\mathbf{v}_S\mathbf{v}_S} & 0 & 0 \\ \Delta t\theta\mathbf{K}_{\mathbf{u}_S\mathbf{u}_S} & \mathbf{M}_{\mathbf{u}_S\mathbf{v}_S} + \theta\Delta t\mathbf{K}_{\mathbf{u}_S\mathbf{v}_S} & \theta\Delta t\mathbf{K}_{\mathbf{u}_S\mathbf{v}_F} & \mathbf{K}_{\mathbf{u}_Sp} \\ 0 & \theta\Delta t\mathbf{K}_{\mathbf{v}_F\mathbf{v}_S} & \mathbf{M}_{\mathbf{v}_F\mathbf{v}_F} + \theta\Delta t\mathbf{K}_{\mathbf{v}_F\mathbf{v}_F} & \mathbf{K}_{\mathbf{v}_Fp} \\ 0 & \mathbf{K}_{\mathrm{pv_S}} & \mathbf{K}_{p\mathbf{v}_F} & 0 \end{pmatrix} \begin{pmatrix} \mathbf{u}_S \\ \mathbf{v}_S \\ \mathbf{v}_F \\ \bar{p} \end{pmatrix}_{n+1} =$$

$$\begin{pmatrix} \mathbf{M}_{\mathbf{v}_S\mathbf{u}_S} & (\theta-1)\Delta t\mathbf{K}_{\mathbf{v}_S\mathbf{v}_S} & 0 & 0 \\ (\theta-1)\Delta t\mathbf{K}_{\mathbf{u}_S\mathbf{u}_S} & \mathbf{M}_{\mathbf{u}_S\mathbf{v}_S} + (\theta-1)\Delta t\mathbf{K}_{\mathbf{u}_S\mathbf{v}_S} & (\theta-1)\Delta t\mathbf{K}_{\mathbf{u}_S\mathbf{v}_F} & 0 \\ 0 & (\theta-1)\Delta t\mathbf{K}_{\mathbf{v}_F\mathbf{v}_S} & \mathbf{M}_{\mathbf{v}_F\mathbf{v}_F} + (\theta-1)\Delta t\mathbf{K}_{\mathbf{v}_F\mathbf{v}_F} & 0 \\ 0 & 0 & 0 & 0 \end{pmatrix} \begin{pmatrix} \mathbf{u}_S \\ \mathbf{v}_S \\ \mathbf{v}_F \\ \bar{p} \end{pmatrix}_n$$

$$+ \theta\Delta t\mathbf{f}_{n+1} + (1-\theta)\Delta t\mathbf{f}_n \tag{16}$$

Note that the time steps (Δt), supposed to be in front of the (blue) pressure matrices, are absorbed into $\bar{p} = \Delta t\, p$, as usually done in CFD, leading to the following saddle-point problem with $\mathbf{U}^T = [\,\mathbf{u}_S^T\, \mathbf{v}_S^T\, \mathbf{v}_F^T\,]$ that we solve for every time step:

$$\begin{pmatrix} \tilde{\mathbf{A}} & \mathbf{B} \\ \mathbf{B}^{\mathrm{T}} & \mathbf{0} \end{pmatrix} \begin{pmatrix} \mathbf{U} \\ \bar{\mathrm{p}} \end{pmatrix}_{n+1} = \mathbf{RHS} \tag{17}$$

After solving the above saddle-point systems, the pressure is scaled back using the relation $p = \bar{p}/\Delta t$. Setting $\theta = \frac{1}{2}$, we recover the second-order Crank-Nicolson scheme (in time), which is based on the well-known trapezoidal rule (TR). However, also fully L-stable 2nd order schemes like BDF(2) or Fractional-Step-Theta-schemes can be used in an analogous way.

3 Numerical validation

To validate and to evaluate our discussed formulations (which all have been realized in our in-house code FEATFLOW[1]), two numerical examples taken from [7] are introduced and implemented in order to compare with well-established methods. Our **uv**p(3)-TR-Q2/P1 approach stands for the described monolithic solver for the **uv**p formulation based

[1] http://www.featflow.de

on the weak forms (7)-(10) using the fully implicit Crank-Nicolson ($\theta = \frac{1}{2}$) time integration scheme as shown in (16) and the mixed finite element pairs Q2/P1 shown in Figure 1. The number 3 in **uv**p(3)-TR-Q2/P1 is used to distinguish our solution algorithms from those in Table I in [7].

3.1 Results I: Saturated poroelastic column under harmonic load

In this example, the response of a homogeneous and isotropic, water-saturated, poroelastic column is analyzed under plane-strain, confined compression conditions. The geometry with boundary conditions and the loading path are illustrated in Figure 2 and the physical parameters, adopted from literature [1], are listed in Table 1.

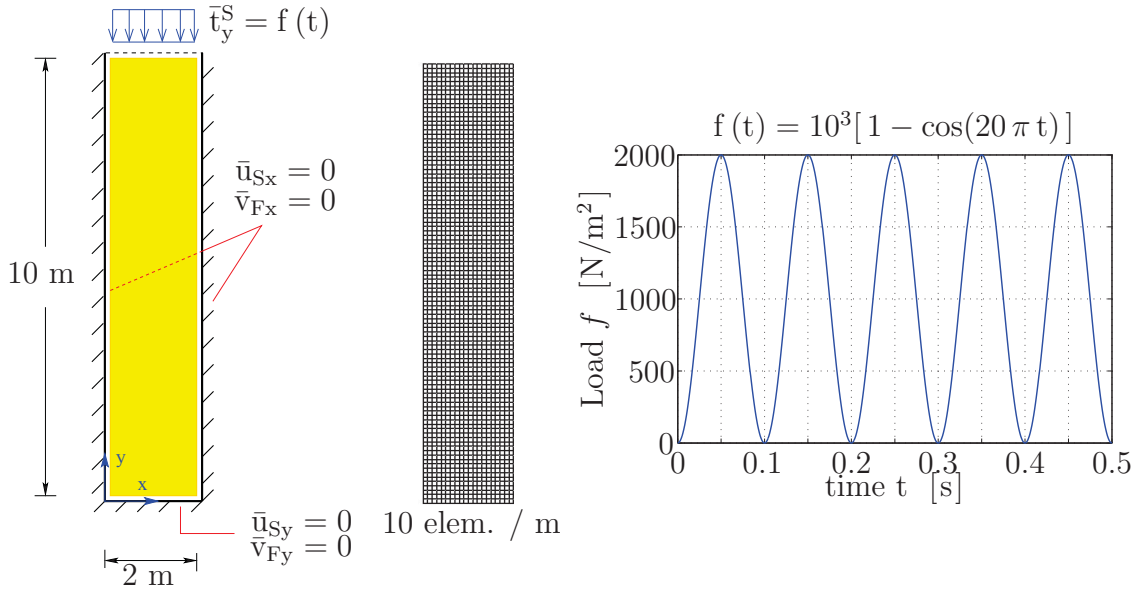

Figure 2: **Left:** Geometry, boundary conditions **Center:** isotropic Cartesian mesh **Right:** loading path of the dynamic confined compression of a saturated poroelastic column.

Table 1: Physical properties of the porous medium used for all simulations.

Parameter	Symbol	Value	SI unit
1st Lamé constant of solid skeleton	μ^S	5.583×10^6	N/m^2
2nd Lamé constant of solid skeleton	λ^S	8.375×10^6	N/m^2
Effective density of dense solid	ρ^{SR}	2000	kg/m^3
Effective density of pore fluid	ρ^{FR}	1000	kg/m^3
Initial volume fraction of solid	$n^S = n^S_{0S}$	0.67	–
Darcy permeability	k^F	10^{-2}, 10^{-5}, 10^{-10}	m/s
Fluid dynamic viscosity (Figure 2 & 4)	ν	10^{-3}	Pa.s
Fluid dynamic viscosity (Figure 7)	ν	10^{-14}	Pa.s

From Figure 3, we notice that, for this problem the proposed **uv**$p(3)$-TR-Q2/P1 method provides almost the most accurate solutions at all selected heights.

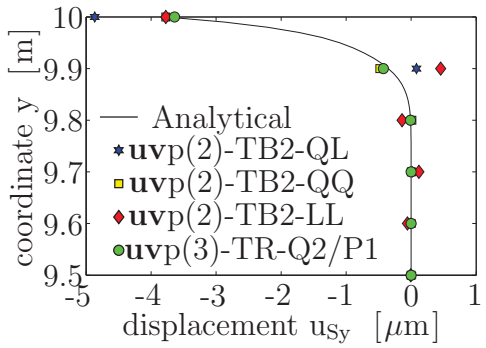

height	LL	QL	QQ	Q2/P1
9.7	0.12	0.019	0.0055	0.0003
9.8	0.13	0.0062	0.0193	0.0010
9.9	0.8	0.43	0.13	0.077
10	0.00	1.1	0.00	0.13

Figure 3: Solid displacement (left) and absolute errors in μm (right) for the first half meter below the top surface for the isotropic Cartesian mesh (10 elem/m) (cf. Figure 2, center) for $k^F = 10^{-5}$m/s at $t = 0.15$ s (All the data except Q2/P1 are taken from [7]).

3.2 Two-dimensional wave propagation

In this second example, we study the 2D dynamical wave propagation in a rectangular symmetric domain under plane-strain conditions (Figure 4) as presented in [2]. The material parameters are the same as before (Table 1) and the 'earthquake event' is represented by the applied distributed impulse force

$$f(t) = 10^5 \, \sin(25\,\pi\,t)\,[1 - H(t-\tau)] \quad [\mathrm{N/m^2}] \tag{18}$$

with $H(t-\tau)$ being the Heaviside step function and $\tau = 0.04\,\mathrm{s}$. The symmetry of the problem can be exploited to reduce the problem size. However, the computation was performed on the full problem for the Q2/P1 approach and extremely low permeability of $\mathrm{k^F} = 10^{-10}$ m/s , which further demonstrates the merits of the considered Q2/P1 approach. For this case both **uv**$p(2)$-TB2-QQ and **uv**$p(2)$-TB2-LL do not converge and the monolithic solution requires LBB-stable mixed FE formulations such as QL [7] and Q2/P1 element pairs. Based on the results shown in Figure 3, the direct comparison between the fully converged QL solutions and the fully converged Q2/P1 solutions (see Figure 5) reveals the less accurate displacement solution of the QL approach. In contrast to the TR-QL approach, our TR-Q2/P1 approach does not produce large pressure oscillations as seen in Figure 6. Such large oscillations are extremely reduced even for the trapezoidal rule (TR) by using a LBB stable element with equal order approximations of $\mathbf{u}_S$, $\mathbf{v}_S$ and $\mathbf{v}_F$ such as the Q2/P1 element.

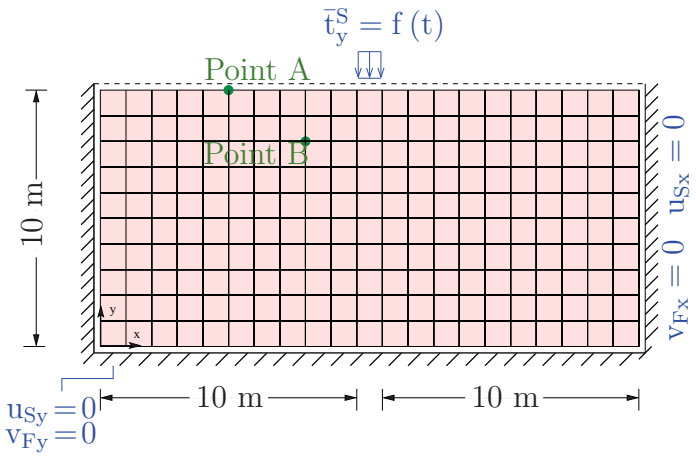

#Elements (width-height)	#DOFs (Q2/P1)	#DOFs (QL)
21-10	6048	3498
42-20	23430	13289
84-40	92214	51771
168-80	365862	102611

Figure 4: Geometry, boundary conditions and mesh level 1 of the symmetric 2D wave propagation problem (left). Total number of elements and unknowns for the **uv**p(3)-TR-Q2/P1 approach (right).

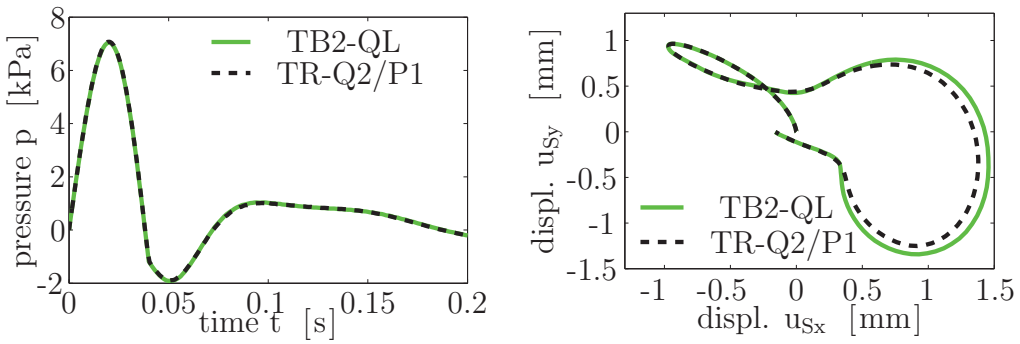

Figure 5: Pressure history at point B and displacement history at point A using **uv**p(3)-TR-Q2/P1 and **uv**p(2)-TB2-QL for $k^F = 10^{-10}$ m/s, $\Delta t = 10^{-3}$ s, $t \in [0\ 0.2]$ s and mesh level 3 for Q2/P1 and QL.

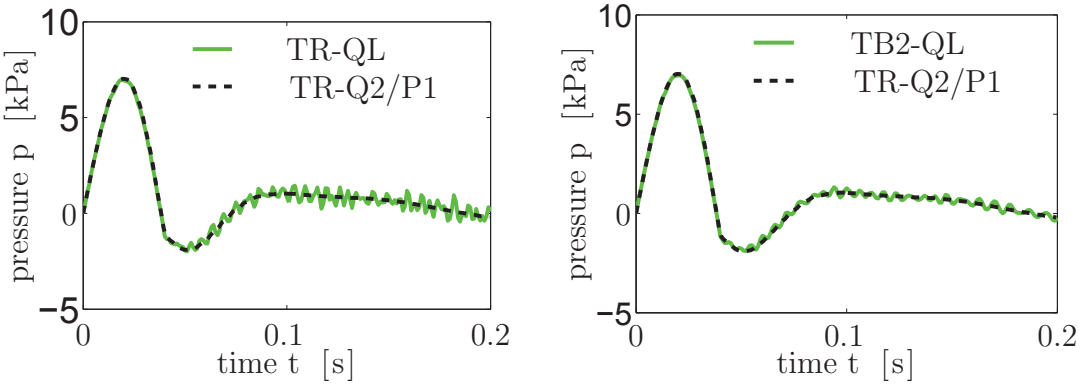

Figure 6: Pressure history at point B for $k^F = 10^{-10}$ m/s, $\Delta t = 10^{-3}$ s and mesh level 2 for **uv**p(3)-TR-Q2/P1, **uv**p(2)-TR-QL and **uv**p(2)-TB2-QL

4 Fast Multigrid solvers

During each time step, most of the elapsed CPU time is consumed by solving the corresponding linear systems in (17). Typically, by accuracy reasons which requires small mesh widths, the arising block systems are too large to be handled by direct solvers, such that iterative schemes have to be preferred. However, due to the nature of the involved partial differential equations, the condition numbers of the arising matrices typically scale with the problem size and are quite large, such that standard single-grid schemes, for instance Krylov-space methods like BICGSTAB or GMRES (cf. [8, 13]), are too slow. Moreover, due to the elliptic character of the incompressibility constraint, the choice of small time steps does not help since the condition numbers do not scale with the time step size due to the incompressibility. Therefore, an excellent alternative is to solve (17) via geometrical multigrid (MG) solvers (see [9, 10, 14]), which require a hierarchy of refined mesh levels and corresponding intergrid transfer operators, which are selected w.r.t. the chosen FEM spaces. What is special for the described saddle-point problems in (17) is the choice of the so-called 'smoothing operator', which in our case can be traced back to the early work by Vanka [12].

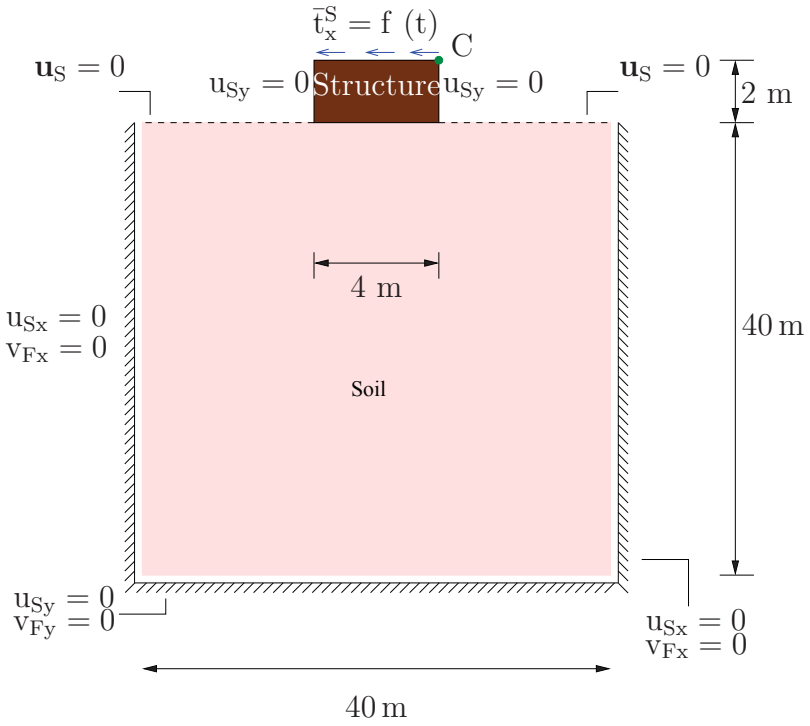

Figure 7: Geometry of the 2D structure-soil problem with prescribed boundary conditions. The domain is composed of a structure, represented by an elastic block ($4 \times 2\ \mathrm{m}^2$) founded on an infinite domain of elastic soil replaced by fixed domain (size: $40 \times 40\ \mathrm{m}^2$) with rigid boundaries. $f(t) = 10^4\,[1 - \cos(20\,\pi\,t)]\,[1 - H(t-\tau)]$ $[\mathrm{N/m}^2]$ with $H(t-\tau)$ being the Heaviside step function and $\tau = 0.1\,\mathrm{s}$ and the material properties are found in Table 1. The time period is set to $t \in [0\ 1.0]\,\mathrm{s}$ and $\Delta t = 2 \times 10^{-3}$.

The corresponding (basic) iterative schemes can be interpreted as block Gauß-Seidel methods applied to mixed formulations of saddle-point problems. In the following, we perform multigrid iterations of F-cycle type, applying a fixed number of pre- and postsmoothing steps for Cartesian (equidistant) grids of the problem depicted in Figure 7. Typically, we will show results for a sequence of consecutively refined meshes, which are constructed by connecting opposite midpoints of the corresponding coarser meshes, starting from a basic mesh on mesh level 1. Sample results, found in Table 2, demonstrate the very efficient convergence behavior for several parameter configurations and they illustrate the typical convergence behavior of multigrid solvers, namely to be more or less independent of the mesh size and the time step.

Table 2: Averaged number of iterations (iter.) and elapsed CPU time (CPU) per time step for the described multigrid solver for **uv**p(3)-TR-Q2/P1 for $t \in [0\ 1.0]$ s and $\Delta t = 2$ ms for the Cartesian grid case.

mesh level	no. elements	no. DOFs	$k^F = 10^{-2}$ m/s		$k^F = 10^{-5}$ m/s		$k^F = 10^{-10}$ m/s	
			iter.	CPU	iter.	CPU	iter.	CPU
2 : (1 elem/m)	1608	44406	2	2.5	2	2	2	2
3 : (2 elem/m)	6432	175638	3	19	3	18	3	18
4 : (4 elem/m)	25728	698598	3	89	2	69	2	70
5 : (8 elem/m)	102912	2786502	3	353	3	348	3	346
6 : (16 elem/m)	411648	11130246	3	1446	3	1440	3	1441

5 Conclusion

Based on the comprehensive investigation of several test cases and the quantitative comparison with the results presented in [7], we recommend our fully implicit, monolithic approach using the uvp(3)-TR-Q2/P1 formulation in combination with the described special multigrid components. The proposed scheme does not only demonstrate excellent numerical results regarding accuracy and robustness, but is also less prone to stability issues (L-stability) of the time integrator even for coarser meshes.

Acknowledgements

We thank Michael Köster for the intensive support in the stage of implementing the presented model into FEATFLOW. Moreover, this work was partially supported by the German Research Foundation (DFG) under grant TU102/34-1.

References

[1] de Boer R, Ehlers W, Liu Z (1993) One-dimensional wave propagation in fluid saturated incompressible porous media. Arch Appl Mech 63:59–72

[2] Breuer S (1999) Quasi-static and dynamic behavior of saturated porous media with incompressible constituents. Transp Porous Media 34:285–303

[3] Diebels S, Ehlers W (1996) Dynamic analysis of a fully saturated porous medium accounting for geometrical and material non-linearities. Int J Numer Methods Eng 39:81–97

[4] Ehlers W (2002) Foundations of multiphasic and porous materials. In: Ehlers W, Bluhm J (eds) Porous Media: Theory, Experiments and Numerical Applications, Springer-Verlag, Berlin, pp 3–86

[5] Heywood J, Rannacher R, Turek S (1996) Artificial boundaries and flux and pressure conditions for the incompressible Navier—-Stokes equations. International Journal for Numerical Methods in Fluids 22(5):325–352

[6] Markert B (2007) A constitutive approach to 3-d nonlinear fluid flow through finite deformable porous continua. Transp Porous Med 70:427–450

[7] Markert B, Heider Y, Ehlers W (2010) Comparison of monolithic and splitting solution schemes for dynamic porous media problem. Int J Numer Meth Eng 82:1341–1383

[8] Saad Y, Schultz M (1986) A generalized minimal residual method for solving nonsymmetric linear systems. SIAM J Sci Statist Comput 7:856–869

[9] Strang G (2007) Computational Science and Engineering. Wellesley-Cambridge press, London

[10] Turek S (1999) Efficient solvers for incompressible flow problems: An algorithmic and computational approach. Springer

[11] Turek S, Hron J, Madlik M, Razzaq M, Wobker H, Acker J (2010) Numerical simulation and benchmarking of a monolithic multigrid solver for fluid–structure interaction problems with application to hemodynamics. In: Bungartz H, Mehl M, Schäfer M (eds) Fluid-Structure Interaction II: Modelling, Simulation, Optimisation, Springer, doi 10.1007/978-3-642-14206-2

[12] Vanka SP (1986) Block-implicit multigrid solution of navier-stokes equations in primitive variables. Journal of Computational Physics 65:138–158

[13] Van der Vorst H (1992) Bi-cgstab: A fast and smoothly converging variant of bi-cg for the solution of nonsymmetric linear systems. SIAM J Sci Stat Comput 13:631–644

[14] Wobker H, Turek S (2009) Numerical studies of Vanka–type smoothers in computational solid mechanics. Advances in Applied Mathematics and Mechanics 1(1):29–55